



Cite this: *Nanoscale*, 2024, **16**, 10663

# Electronic redistribution through the interface of $\text{MnCo}_2\text{O}_4$ – $\text{Ni}_3\text{N}$ nano-urchins prompts rapid *in situ* phase transformation for enhanced oxygen evolution reaction†

Ashish Gaur,<sup>‡</sup> Aashi,<sup>‡</sup> Joel Mathew John, Vikas Pundir, Rajdeep Kaur, Jatin Sharma, Kaustubhi Gupta, Chandan Bera  and Vivek Bagchi \*

One of the most coveted objectives in the realm of energy conversion technologies is the development of highly efficient and economically viable electrocatalysts for the oxygen evolution reaction. The commercialization of such techniques has thus far been impeded by their slow response kinetics. One of the many ways to develop highly effective electrocatalysts is to judiciously choose a coupling interface that maximizes catalyst performance. In this study, the *in situ* electrochemical phase transformation of  $\text{MnCo}_2\text{O}_4$ – $\text{Ni}_3\text{N}$  into  $\text{MnCo}_2\text{O}_4$ – $\text{NiOOH}$  is described. The catalyst has an exceptional overpotential of 224 mV to drive a current density of  $10 \text{ mA cm}^{-2}$ . Strong interfacial contact is seen in the  $\text{MnCo}_2\text{O}_4$ – $\text{Ni}_3\text{N}$  catalyst, leading to a considerable electronic redistribution between the  $\text{MnCo}_2\text{O}_4$  and  $\text{Ni}_3\text{N}$  phases. This causes an increase in the valence state of Ni, which makes it an active site for the adsorption of  $^*\text{OH}$ ,  $\text{O}^*$ , and  $^*\text{OOH}$  (intermediates). This charge transfer facilitates the rapid phase transformation to form  $\text{NiOOH}$  from  $\text{Ni}_3\text{N}$ . At a higher current density of  $300 \text{ mA cm}^{-2}$ , the catalyst remained stable for a period of 140 h. DFT studies also revealed that the *in situ*-formed  $\text{NiOOH}$  on the  $\text{MnCo}_2\text{O}_4$  surface results in superior OER kinetics compared to that of  $\text{NiOOH}$  alone.

Received 6th February 2024,  
Accepted 30th April 2024

DOI: 10.1039/d4nr00560k

rsc.li/nanoscale

## Introduction

We have never been more susceptible to the potentially disastrous repercussions of climate change than we are right now. A dramatic change in both the temperature and the pattern of the weather has resulted as a direct consequence of severe human activities such as warfare, vast space exposition, and numerous other steps that emit greenhouse gases. This has resulted in significant dangers to all forms of life on the planet.<sup>1</sup> Hence, it is vital to solve the ever-increasing petrochemical energy crises and environmental pollution concerns by creating sustainable and green energy sources.<sup>2–5</sup> For oxygen/hydrogen production, electrocatalytic water splitting has attracted great attention. However, the sluggishness of the reaction kinetics of the oxygen evolution reaction (OER) and its complex reaction mechanism are barriers to the water splitting reaction.<sup>6–8</sup> In general, the OER entails a multi-step four-electron transfer.<sup>9–12</sup> It is still difficult to speed up the electron

transfer process in the OER at the same time by merely changing the charge of the electrocatalyst.<sup>13,14</sup> Recently, first-row transition metal-based spinel oxides have been widely investigated as potential materials for OER due to their excellent durability under elevated anodic potential and the interaction of their inner multivalent states.<sup>15,16</sup> The existence of tetrahedral and octahedral sites in the spinel structure offers numerous locations for accommodating various transition-metal cations in a variety of valence states to generate a substantial number of oxides.<sup>17–20</sup> In all the spinel oxides, the intrinsic conductivity is very low due to their semiconducting nature and the small number of active sites.<sup>21,22</sup> Recent theoretical and experimental investigations have already shown that  $\text{Ni}_3\text{N}$  is a very intriguing material in this scenario, since it has certain surface terminations and crystal facets that can provide optimal energetics for water dissociation.<sup>23–25</sup> Different fabrications of metal-nitride-based electrocatalysts have been developed to further increase the effectiveness of the water splitting performance of metal nitrides such as  $\text{Ni}_3\text{N}$ – $\text{NiMoN/CC}$ ,  $\text{Ru/Ni}_3\text{N}$ – $\text{Ni}$  and  $\text{Co-Ni}_3\text{N}$ .<sup>26–28</sup> In all these materials, the Ni atoms have a low oxidation state, which makes them electron-rich with a filled  $e_g$  orbital. However, the activity of the Ni-based materials can be further enhanced by the enhanced valence state of the Ni atoms. Higher-valent Ni metal atoms can

Institute of Nano Science and Technology, Sector-81, Knowledge City, Sahibzada Ajit Singh Nagar, Punjab, Pin – 140306, India. E-mail: bagchiv@inst.ac.in

† Electronic supplementary information (ESI) available. See DOI: <https://doi.org/10.1039/d4nr00560k>

‡ Both the authors contributed equally.

tremendously enhance the OER by enhancing the rate of adsorption of intermediates ( $\text{OH}^*$ ,  $\text{O}^*$  and  $\text{OOH}^*$ ) on the active sites.<sup>29–32</sup> Interface coupling has a significant effect on electrocatalytic behaviour through electronic modulation of the surface atoms present at the interface, adjusting the overlap of orbitals between different atoms, and ultimately optimizing the attachment of the intermediates on the electrode surface.<sup>33–37</sup>

Meanwhile, the findings of theoretical simulations and experimental characterizations have shown that the *in situ* formed metal oxyhydroxides on the outermost layer of metal nitrides are active species that accelerate the OER kinetics.<sup>38,39</sup> As an illustration, Schuhmann and his coworkers demonstrated that the conversion of  $\text{Co}_2\text{N}$  into more active  $\text{CoOOH}$  can boost the OER kinetics.<sup>40</sup> Therefore, choosing the appropriate solid for  $\text{Ni}_3\text{N}$  to develop a composition in which the interfacial interaction can significantly enhance the phase transformation of the  $\text{Ni}_3\text{N}$  phase to construct the more-active  $\text{NiOOH}$  phase.

Herein, using the interfacial interaction technique, we formed novel heterointerfaces of  $\text{MnCo}_2\text{O}_4$ – $\text{Ni}_3\text{N}$  over nickel foam (Scheme 1). The electrodeposition technique was used for the synthesis of  $\text{Ni}(\text{OH})_2$  nanosheets over  $\text{MnCo}_2\text{O}_4$  nanowires. Further nitridation in the presence of ammonia produces the  $\text{Ni}_3\text{N}$  nanosheets over the  $\text{MnCo}_2\text{O}_4$  nanowire scaffold. The heterostructure undergoes rapid phase transformation to generate more efficient  $\text{NiOOH}$  species. This heterostructure shows impressive OER activity, achieving an overpotential of 224 mV (@ 10  $\text{mA cm}^{-2}$ ). The durability of the catalyst is also excellent, with no change in current density (300  $\text{mA cm}^{-2}$ ) even after 140 h of stability testing. Charge transfer from  $\text{Ni}_3\text{N}$  to  $\text{MnCo}_2\text{O}_4$  has been observed and characterized using X-ray photoelectron spectroscopy (XPS). The presence of high-valent  $\text{Mn}^{3+}$  and  $\text{Co}^{3+}$  in  $\text{MnCo}_2\text{O}_4$  makes it of high polarity, which results in electronic uptake from the  $\text{Ni}_3\text{N}$  phase through the interface. This reallocation of electrons through the interface leads to the enhancement of the Ni valence state and enhances the adsorption of  $\text{OH}^-$  ions, which

simultaneously increases the catalytic performance towards the oxygen evolution reaction (OER) by reconstructing the phase to form more active  $\text{NiOOH}$  species. We have also carried out DFT calculations of the  $\text{MnCo}_2\text{O}_4$ – $\text{NiOOH}$  heterostructure, and the results showed that the  $\text{NiOOH}$  that is created over the surface of  $\text{MnCo}_2\text{O}_4$  possesses a higher level of activity compared to  $\text{NiOOH}$  alone.

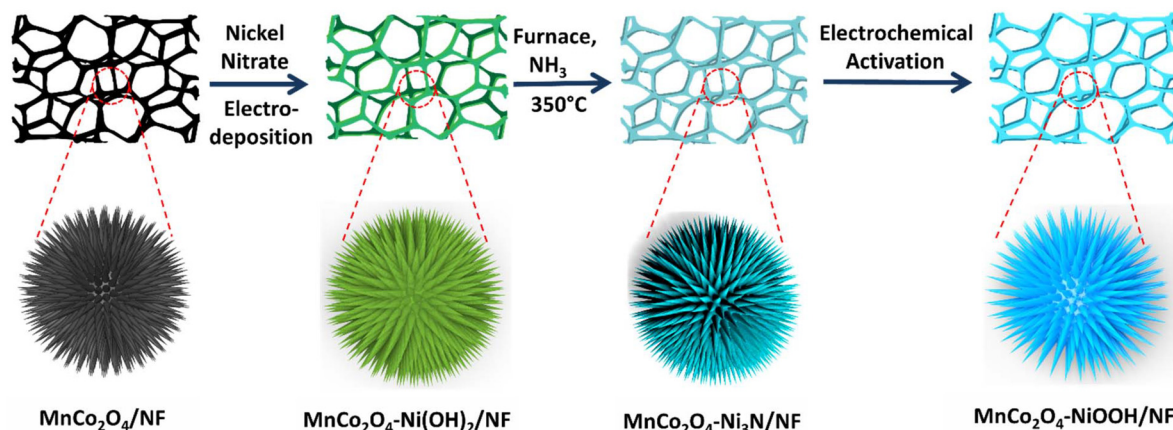
## Experimental section

### Materials

All chemicals are purchased from a variety of sources and utilised in their original forms. Manganese(II) chloride tetrahydrate ( $\text{MnCl}_2 \cdot 4\text{H}_2\text{O}$ , 99.9%), cobalt(II) nitrate hexahydrate ( $\text{Co}(\text{NO}_3)_2 \cdot 6\text{H}_2\text{O}$ , 98%), nickel(II) nitrate hexahydrate ( $\text{Ni}(\text{NO}_3)_2 \cdot 6\text{H}_2\text{O}$ , 98%), ammonium fluoride ( $\text{NH}_4\text{F}$ , 99.9%), urea ( $\text{NH}_2\text{CONH}_2$ , 99.5%), potassium hydroxide pellets ( $\text{KOH}$ ) and ruthenium(IV) oxide ( $\text{RuO}_2$ , 99.9% trace metal basis) were purchased from Sigma Aldrich. Nanoshel was the supplier of nickel foam (NF). For every step of the preparation, Milli-Q water with a conductivity of 0.056  $\text{S cm}^{-1}$  was used.

### Synthesis of $\text{MnCo}_2\text{O}_4$ nanowires on NF

To cleanse the surface and remove any unwanted coatings, the NF was gently washed with DI water and acetone after being cleaned with a 3 M HCl solution that was ultrasonically agitated. The cleaned NF was divided into small pieces with a 1 cm  $\times$  1.5 cm cross-sectional area. The hydrothermal method was used to grow nanowires of  $\text{MnCo}_2\text{O}_4$ . A homogeneous solution of 0.280 g  $\text{Co}(\text{NO}_3)_2 \cdot 6\text{H}_2\text{O}$ , 0.088 g  $\text{MnCl}_2 \cdot 4\text{H}_2\text{O}$ , 0.068 g  $\text{NH}_4\text{F}$ , and 0.051 g urea was made using 5 mL of ethanol and 25 mL of DI water. The above-described solution was placed in a Teflon-lined stainless-steel autoclave, and one piece of NF was placed in the autoclave. The autoclave was heated at 120  $^\circ\text{C}$  for 12 h. The as-synthesized  $\text{MnCoLDH/NF}$  was removed from the autoclave and rinsed with ethanol and DI water. After washing, the electrode was dried at 60  $^\circ\text{C}$  over-



**Scheme 1** Formation of  $\text{MnCo}_2\text{O}_4$ – $\text{NiOOH}$  nano-urchins over nickel foam.

night. Finally, the as-prepared MnCoLDH/NF electrode was calcined in air for 2 hours at 350 °C to form MnCo<sub>2</sub>O<sub>4</sub> over nickel foam.

### Synthesis of MnCo<sub>2</sub>O<sub>4</sub>-Ni<sub>3</sub>N

Nickel hydroxide nanosheets were electrodeposited over MnCo<sub>2</sub>O<sub>4</sub>/NF. The fabrication of Ni(OH)<sub>2</sub> was done using a three-electrode setup in which MnCo<sub>2</sub>O<sub>4</sub>/NF, Ag/AgCl, and graphite rod were used as the working, reference, and counter electrodes, respectively. The electrolyte was prepared using an aqueous solution of 0.2 M Ni(NO<sub>3</sub>)<sub>2</sub>·6H<sub>2</sub>O. The deposition potential was kept at -2.0 V for 600 seconds. Following this step, the deposition of Ni(OH)<sub>2</sub> onto the MnCo<sub>2</sub>O<sub>4</sub>/NF substrate occurred. This MnCo<sub>2</sub>O<sub>4</sub>-Ni(OH)<sub>2</sub> electrode was heated in a furnace at 350 °C under a constant NH<sub>3</sub> flow for 2 h. Ni(OH)<sub>2</sub> was transformed into Ni<sub>3</sub>N sheets over the MnCo<sub>2</sub>O<sub>4</sub> nanowire. The obtained MnCo<sub>2</sub>O<sub>4</sub>-Ni<sub>3</sub>N catalyst was washed with DI and ethanol several times and used as a working electrode. The synthesis of MnCo<sub>2</sub>O<sub>4</sub> and Ni<sub>3</sub>N individually, along with the physical characterization and electrochemical analysis details, are provided in ESI S1.1 and 1.2.†

### Synthesis of MnCo<sub>2</sub>O<sub>4</sub>-NiOOH

MnCo<sub>2</sub>O<sub>4</sub>-NiOOH was fabricated *in situ* through anodic oxidation of the MnCo<sub>2</sub>O<sub>4</sub>-Ni<sub>3</sub>N. A three-electrode setup was used, in which a graphite rod was the counter electrode, Ag/AgCl was the reference electrode and MnCo<sub>2</sub>O<sub>4</sub>-Ni<sub>3</sub>N was used as a working electrode. In addition, 1 M KOH was used as the electrolyte. The catalyst was formed by conducting 50 LSV cycles in the potential range of 0 to 1 V (vs. RHE). The scan rate was kept at 5 mV s<sup>-1</sup>. The phase transformation of MnCo<sub>2</sub>O<sub>4</sub>-Ni<sub>3</sub>N occurred to give MnCo<sub>2</sub>O<sub>4</sub>-NiOOH.

## Results and discussion

As shown in Scheme 1, the catalyst MnCo<sub>2</sub>O<sub>4</sub>-Ni<sub>3</sub>N was produced using the temperature-controlled nitridation of MnCo<sub>2</sub>O<sub>4</sub>-Ni(OH)<sub>2</sub> under the indicated conditions. Electron transport between Ni<sub>3</sub>N and MnCo<sub>2</sub>O<sub>4</sub> is facilitated by the presence of a heterointerface between the two materials. NiOOH is produced from Ni<sub>3</sub>N upon electrochemical activation and can catalyse the oxygen evolution reaction (OER). Structural elucidation of all the catalysts was conducted using PXRD analysis. The PXRD pattern of MnCo<sub>2</sub>O<sub>4</sub>-Ni<sub>3</sub>N is shown in Fig. 1a. This pattern confirms the formation of MnCo<sub>2</sub>O<sub>4</sub> and Ni<sub>3</sub>N with a set of obvious diffraction peaks corresponding to the cubic and hexagonal phases of MnCo<sub>2</sub>O<sub>4</sub> (JCPDS No. 23-1237) and Ni<sub>3</sub>N (JCPDS No. 70-9598), respectively.<sup>41-43</sup> The electronic structure, chemical states, and electronic redistribution in MnCo<sub>2</sub>O<sub>4</sub>-Ni<sub>3</sub>N, MnCo<sub>2</sub>O<sub>4</sub> and, Ni<sub>3</sub>N were investigated using X-ray photoelectron spectroscopy analysis (XPS). The wide-scan XPS spectra of MnCo<sub>2</sub>O<sub>4</sub>-Ni<sub>3</sub>N, MnCo<sub>2</sub>O<sub>4</sub>, and Ni<sub>3</sub>N can be found in ESI S2.1 Fig. S1.† We observed three peaks in the Ni 2p spectrum of MnCo<sub>2</sub>O<sub>4</sub>-Ni<sub>3</sub>N (Fig. 1b), with centres located at 853.2, 856.3, and 860.7 eV, respectively. These peaks are

attributed to the existence of Ni-N and Ni-O, in addition to one satellite peak of Ni 2p<sub>3/2</sub>. Furthermore, the presence of all three peaks is also evident in the context of Ni2p<sub>1/2</sub> splitting at 870.5, 873.6, and 878.6 eV.<sup>27,44</sup> These peaks can also be seen in the Ni 2p XPS spectra of Ni<sub>3</sub>N alone (Fig. 1b), but at a somewhat lower binding energy. The increased binding energy of Ni 2p in MnCo<sub>2</sub>O<sub>4</sub>-Ni<sub>3</sub>N implies that charge is being transferred from Ni to another atom. The N 1s spectrum (Fig. 1c) for MnCo<sub>2</sub>O<sub>4</sub>-Ni<sub>3</sub>N shows a peak at 398.7 eV, which is attributed to the metal-nitrogen bond.<sup>45,46</sup> The N 1s spectra of Ni<sub>3</sub>N exhibits the peak for the M-N bond at a significantly lower binding energy.

The investigation was further extended to the Mn2p XPS spectra of MnCo<sub>2</sub>O<sub>4</sub>-Ni<sub>3</sub>N and MnCo<sub>2</sub>O<sub>4</sub>. We observed four peaks in the Mn2p spectrum of the catalyst at 640.0, 641.3, 652.1, and 652.2 eV corresponding to the Mn<sup>2+</sup> and Mn<sup>3+</sup> peaks of Mn2p<sub>3/2</sub> and Mn2p<sub>1/2</sub> splitting (Fig. 1d). All four peaks are also detected in the Mn2p spectrum of MnCo<sub>2</sub>O<sub>4</sub> alone, but at higher binding energy. Similarly, in the Co2p XPS spectrum of MnCo<sub>2</sub>O<sub>4</sub>-Ni<sub>3</sub>N, we observed three peaks at 779.1, 781.6, and 785.7 eV for Co<sup>3+</sup>, Co<sup>2+</sup>, and one satellite peak of Co2p<sub>3/2</sub> splitting (Fig. 1e). The other three peaks at 795.0, 796.9 and 801.7 eV correspond to Co<sup>3+</sup>, Co<sup>2+</sup> and one satellite peak of Co2p<sub>1/2</sub> splitting.<sup>47,48</sup> Similarly, the Co2p spectra of pure MnCo<sub>2</sub>O<sub>4</sub> show all six peaks, but with a higher binding energy. Even the O 1s spectrum showed this same pattern (Fig. 1f). The O 1s spectrum of MnCo<sub>2</sub>O<sub>4</sub>-Ni<sub>3</sub>N shows three peaks labelled as O1, O2, and O3 at 528.8, 530.4, and 532.0 eV. The peaks O1 and O2 correspond to the presence of O<sup>2-</sup>, which is indicative of the formation of spinel MnCo<sub>2</sub>O<sub>4</sub>.<sup>49-51</sup> The peak O3 corresponds to the presence of chemisorbed oxygen. These three peaks are consistent with the O 1s spectra of pure MnCo<sub>2</sub>O<sub>4</sub>, but are found at higher binding energies. The shift towards higher binding energies for Ni and N and the shift towards lower binding energy in the case of Mn, Co, and O confirms the charge transfer from Ni<sub>3</sub>N to MnCo<sub>2</sub>O<sub>4</sub>. As a result of the valence-state enhancement of Ni caused by the transfer of charges, the Ni surfaces become excellent adsorption sites for O\*, \*OH and HOO\* intermediate species. This rapid adsorption of intermediates is responsible for the rapid phase transformation of Ni<sub>3</sub>N into NiOOH, which further enhances the reaction kinetics for the OER. The conversion of Ni<sub>3</sub>N to NiOOH was further confirmed from the XPS spectra. The peak corresponding to the existence of Ni-N disappeared (Fig. 1g). The XPS spectra of Co2p (Fig. 1h) and Mn2p (Fig. 1i) remained the same, as there was no change in the MnCo<sub>2</sub>O<sub>4</sub> phase. The XPS spectra of O 1s is provided in ESI S2.2 Fig. S2.†

To understand the morphology of the MnCo<sub>2</sub>O<sub>4</sub>-Ni<sub>3</sub>N catalyst, FESEM analysis was carried out at each step. We observed the fine nanowires of MnCo<sub>2</sub>O<sub>4</sub> collectively formed a nano-urchin-like morphology (Fig. 2a and b). Subsequently, fine nanosheets of Ni<sub>3</sub>N were grown over the surface of the MnCo<sub>2</sub>O<sub>4</sub> nanowires. The MnCo<sub>2</sub>O<sub>4</sub>-Ni<sub>3</sub>N nano-urchins are depicted in Fig. 2c and d. During the OER, the Ni<sub>3</sub>N phase was converted into NiOOH, and the surface of the nano-urchins also became rough due to the presence of more exposed



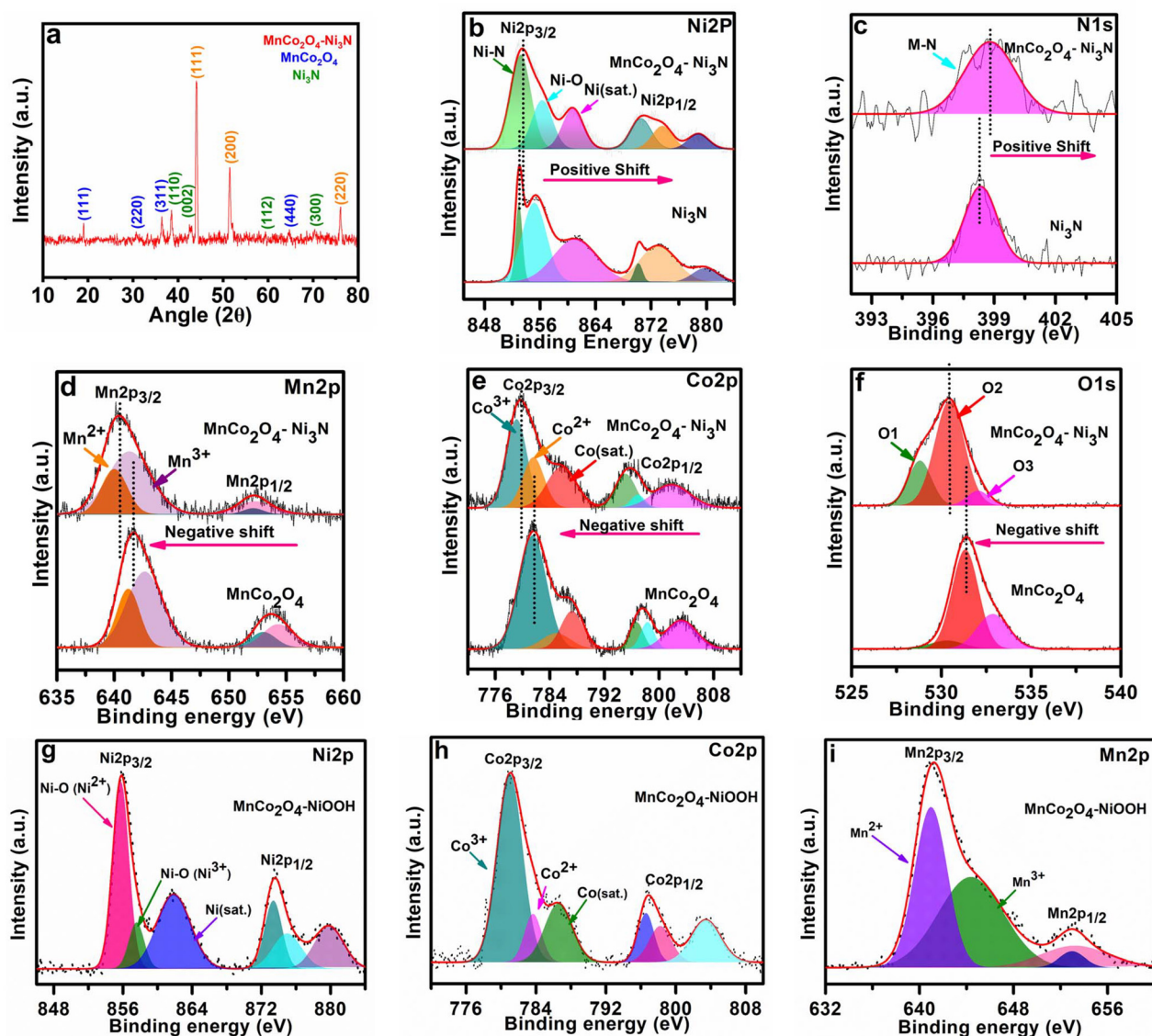


**Fig. 1** (a) PXRD pattern of  $\text{MnCo}_2\text{O}_4\text{-Ni}_3\text{N}$ . High-resolution (b) Ni2p present in  $\text{MnCo}_2\text{O}_4\text{-Ni}_3\text{N}$  and  $\text{Ni}_3\text{N}$ . (c) N1s present in  $\text{MnCo}_2\text{O}_4\text{-Ni}_3\text{N}$  and  $\text{Ni}_3\text{N}$ . (d) Mn2p, (e) Co2p and (f) O1s present in  $\text{MnCo}_2\text{O}_4\text{-Ni}_3\text{N}$  and  $\text{MnCo}_2\text{O}_4$ . (g) Ni2p (h) Co2p and (i) Mn2p XPS spectra of  $\text{MnCo}_2\text{O}_4\text{-NiOOH}$ .

NiOOH on the surface. The SEM images of  $\text{MnCo}_2\text{O}_4\text{-NiOOH}$  are provided in Fig. 2e and f.

Examination with a transmission electron microscope (TEM) was also carried out to gain additional understanding regarding the shape and microstructure of the  $\text{MnCo}_2\text{O}_4\text{-NiOOH}$  catalysts. Fig. 3a shows the TEM image of a  $\text{MnCo}_2\text{O}_4$  nanowire, whereas the presence of NiOOH nanosheets over the surface of  $\text{MnCo}_2\text{O}_4$  nanowires can be seen in Fig. 3b and c. To confirm the presence of  $\text{MnCo}_2\text{O}_4$  and NiOOH in the catalyst, HRTEM analysis was carried out. Fig. 3d–f show an HRTEM image of the catalyst with fringe widths of 0.25 and 0.22 nm corresponding to the (311) plane of  $\text{MnCo}_2\text{O}_4$  and (102) plane of NiOOH.<sup>41</sup>

The phenomenon of superhydrophilicity, which is characterized by a the strong affinity of a surface for water, resulting

in a thin dispersion of water and the absence of droplet formation, can exert a substantial impact on the electrocatalytic processes. Efficient contact between the catalyst surface and the electrolyte is crucial for electrolysis and other electrochemical reactions. The impact of superhydrophilicity on electrocatalysis can be explained by the enhanced surface wettability, increased mass transport and reduction in concentration polarization.<sup>52–54</sup> The contact angle of the surface of bare nickel foam was measured to be  $116.7^\circ$ , making it hydrophobic (ESI S3 Fig. S3.1†). On the other hand, the surface of  $\text{MnCo}_2\text{O}_4\text{-NiOOH}$  was found to have a contact angle of  $0^\circ$ , making it superhydrophilic (Fig. 3g and h). We also analyzed the surface behaviour of the  $\text{MnCo}_2\text{O}_4$  and NiOOH; the  $\text{MnCo}_2\text{O}_4$  was found to be hydrophobic, whereas the surface of the NiOOH was found to be superhydrophilic (ESI S3.2

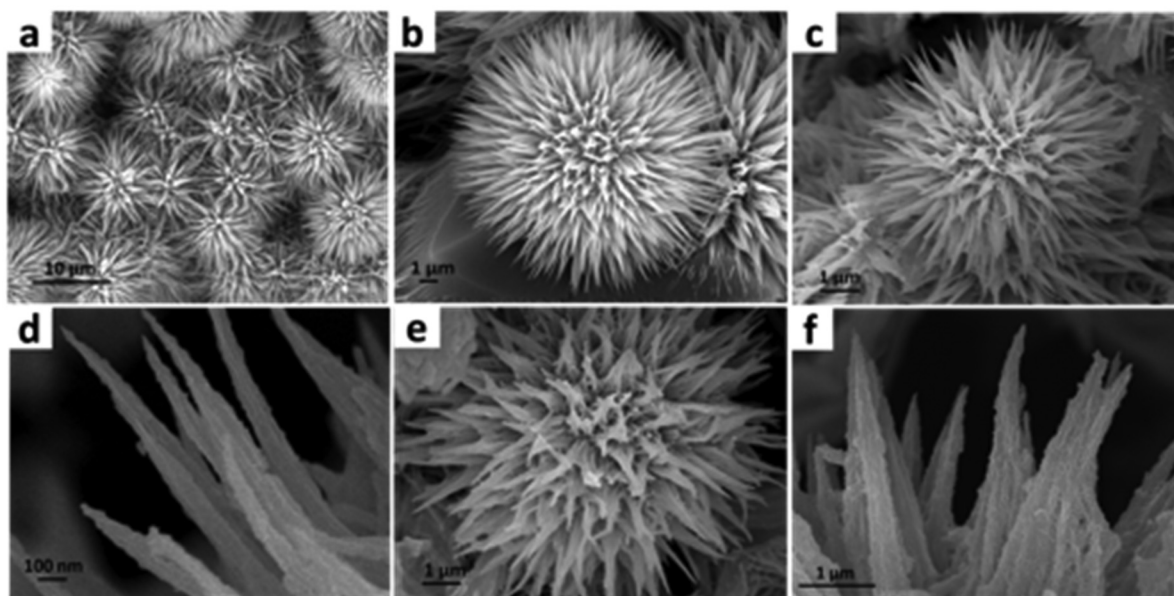


**Fig. 2** (a) and (b) FESEM images of MnCo<sub>2</sub>O<sub>4</sub> nano-urchins at different magnifications. (c) and (d) Ni<sub>3</sub>N grown over MnCo<sub>2</sub>O<sub>4</sub> nano-urchins. (e) and (f) NiOOH grown over MnCo<sub>2</sub>O<sub>4</sub> nano-urchins.

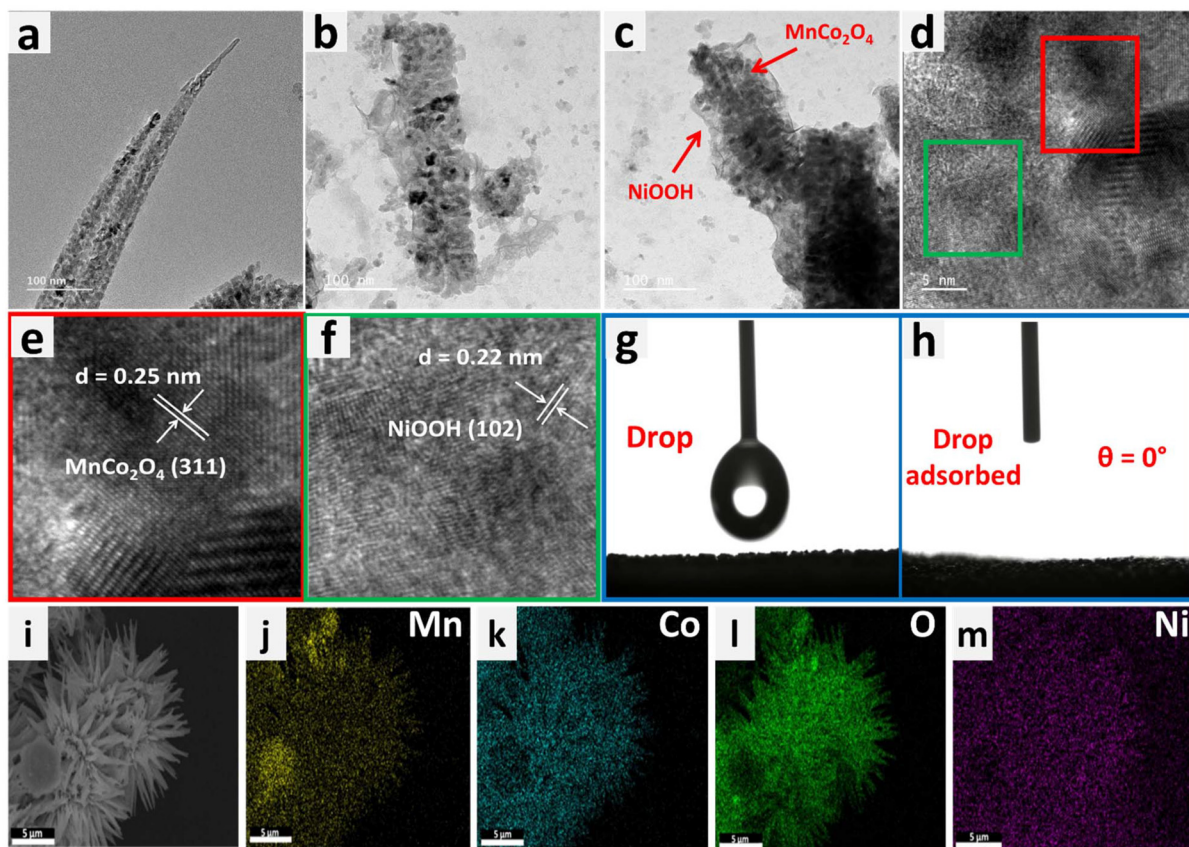


**Fig. 3** (a) TEM images of a MnCo<sub>2</sub>O<sub>4</sub> nanowire and (b) and (c) NiOOH nanosheets grown over a MnCo<sub>2</sub>O<sub>4</sub> nanowire. (d) HRTEM image of MnCo<sub>2</sub>O<sub>4</sub>-NiOOH confirming the presence of (e) MnCo<sub>2</sub>O<sub>4</sub> and (f) NiOOH. (g) and (h) Hydrophilicity analysis using drop shape analysis for MnCo<sub>2</sub>O<sub>4</sub>-NiOOH. (i) Image on which elemental mapping was carried out and the fine distributions of (j) Mn, (k) Co, (l) Ni and (m) O.



Fig. S4†). The even distribution of Mn, Co, Ni, and O over the catalyst scaffold was verified using FESEM elemental mapping (Fig. 3(i)–(m)).

### Electrochemical

After the catalysts were developed, further studies were carried out in an aqueous electrolyte using a three-electrode setup to investigate the electrocatalytic capabilities of the catalysts in the oxygen evolution reaction (OER). The catalyst was generated *in situ* by conducting linear sweep voltammetry in the potential range of 1 to 2 V (vs. RHE). The  $\text{MnCo}_2\text{O}_4\text{-Ni}_3\text{N}$  electrode was transformed rapidly into the  $\text{MnCo}_2\text{O}_4\text{-NiOOH}$  electrode as soon as the OER process started. This rapid phase modification of  $\text{MnCo}_2\text{O}_4\text{-Ni}_3\text{N}$  into  $\text{MnCo}_2\text{O}_4\text{-NiOOH}$  is due to the strong interfacial contact within the  $\text{MnCo}_2\text{O}_4$  and  $\text{Ni}_3\text{N}$  phase. We confirmed this by the position of the oxidation peak of Ni ( $\text{Ni}^{2+} \rightarrow \text{Ni}^{3+}$ ). The position of the oxidation peak is at 1.40 V (vs. RHE) for the oxidation of the bare  $\text{Ni}_3\text{N}$  electrode,

whereas for the heterostructure  $\text{MnCo}_2\text{O}_4\text{-Ni}_3\text{N}$  it is at 1.33 V (vs. RHE) (Fig. 4a). This shows that the potential required for the oxidation of the  $\text{Ni}_3\text{N}$  present in  $\text{MnCo}_2\text{O}_4\text{-Ni}_3\text{N}$  is much lower than that of the pure  $\text{Ni}_3\text{N}$  phase. Fig. 4b shows the polarization curves of  $\text{MnCo}_2\text{O}_4\text{-NiOOH}$ ,  $\text{MnCo}_2\text{O}_4$ ,  $\text{NiOOH}$  and commercially available  $\text{RuO}_2$ .

At a current density of  $10 \text{ mA cm}^{-2}$ , an overpotential of 224, 270, 300, and 350 mV was obtained for  $\text{MnCo}_2\text{O}_4\text{-NiOOH}$ ,  $\text{RuO}_2$ ,  $\text{MnCo}_2\text{O}_4$ , and  $\text{NiOOH}$ , respectively. The  $\text{MnCo}_2\text{O}_4\text{-NiOOH}$  heterostructure outperforms  $\text{RuO}_2$  as well as all the supporting catalysts at all current densities. Fig. 4c provides an insightful comparison of the overpotential at a current density of  $10 \text{ mA cm}^{-2}$  for all the catalysts. To gain a deeper comprehension of the kinetics of the catalysts, the value of the Tafel slope was determined by linear fitting of the polarization curve (Fig. 4d). A Tafel slope value of  $111 \text{ mV dec}^{-1}$  is obtained for the  $\text{MnCo}_2\text{O}_4\text{-NiOOH}$  heterostructure, which is lower than those of  $\text{RuO}_2$  ( $115 \text{ mV dec}^{-1}$ ),  $\text{NiOOH}$  ( $142 \text{ mV dec}^{-1}$ ) and

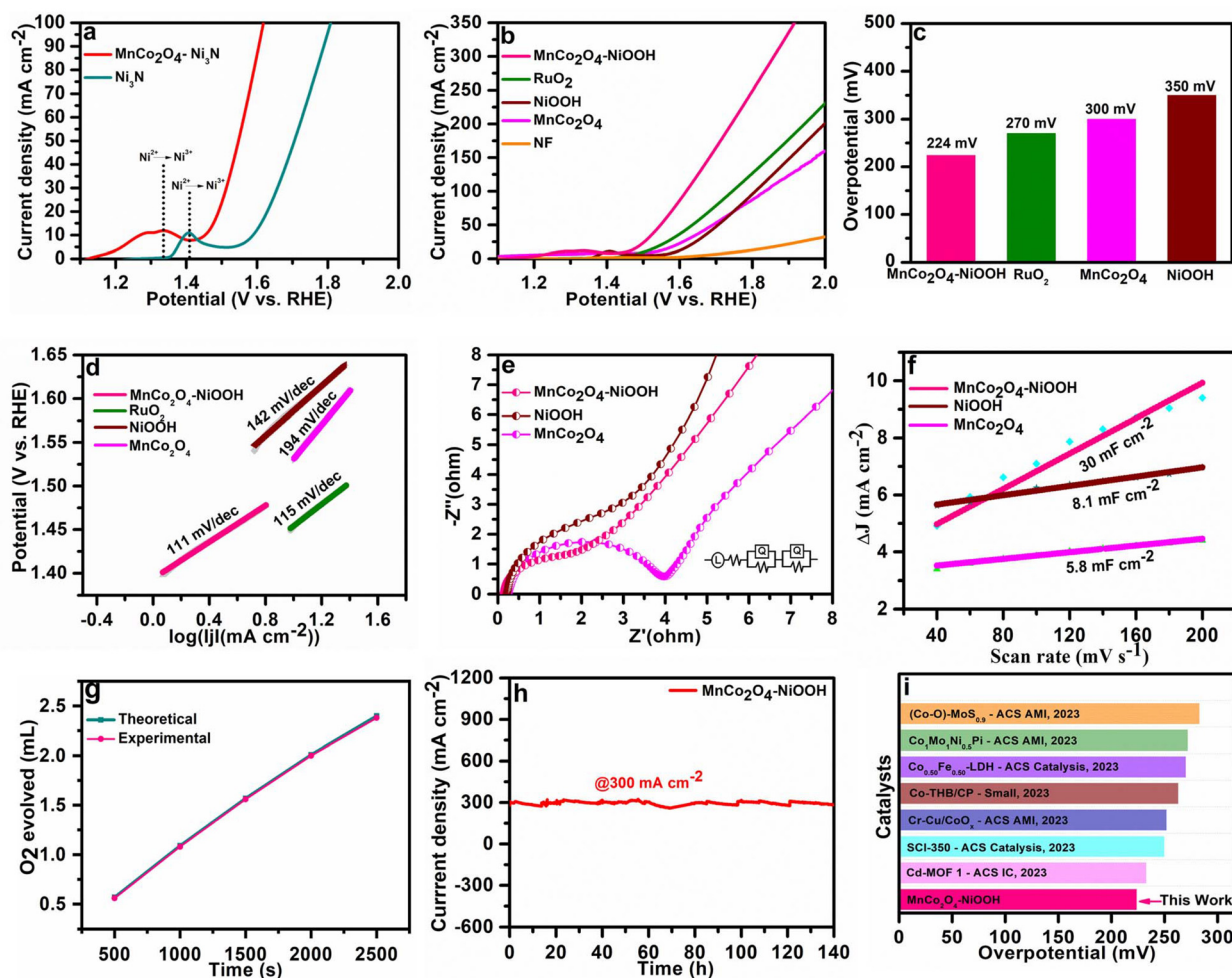


Fig. 4 (a) Polarization curve showing the position of the oxidation peak. (b) Polarization curve for the OER activity of  $\text{MnCo}_2\text{O}_4\text{-NiOOH}$  and other supporting catalysts. (c) Overpotential at  $10 \text{ mA cm}^{-2}$  of current density. (d) Tafel slope values of all the catalysts. (e) EIS Nyquist plots and (f) double layer capacitance of  $\text{MnCo}_2\text{O}_4\text{-NiOOH}$ ,  $\text{NiOOH}$  and  $\text{MnCo}_2\text{O}_4$ . (g) Faradic efficiency of  $\text{MnCo}_2\text{O}_4\text{-NiOOH}$ . (h) Stability study using chronoamperometry. (i) Overpotential comparison with recently reported catalysts.

$\text{MnCo}_2\text{O}_4$  ( $194 \text{ mV dec}^{-1}$ ). The smaller Tafel slope value of the catalyst implies that the heterostructure likely exhibits quicker reaction kinetics than the separate phases.

Electrochemical impedance spectroscopy was used to assess the charge transfer resistance to estimate the interfacial interaction necessary for quicker electron transfer over the interface of electrode and electrolyte. The Nyquist plots of  $\text{MnCo}_2\text{O}_4$ -NiOOH, NiOOH and  $\text{MnCo}_2\text{O}_4$  at 200 mV of overpotential are provided in Fig. 4e. The  $\text{MnCo}_2\text{O}_4$ -NiOOH heterostructure exhibited a lower  $R_{\text{ct}}$  value. This lower value of  $R_{\text{ct}}$  implies that there are a significant number of electrochemically active sites on the surface of the electrode, and that there is also a significant amount of interfacial charge transfer. These outcomes from the Nyquist plot indicate that there is a considerable increase in OER activity as well. We examined the electrochemical  $C_{\text{dl}}$  of the  $\text{MnCo}_2\text{O}_4$ -NiOOH catalyst to obtain an accurate evaluation of the OER activity that is inherently present in the reported catalyst. The  $C_{\text{dl}}$  was calculated using cyclic voltammetry scans performed between 0.01 to 0.1 V (V vs. Ag/AgCl) with varying scan rates of 20 to 200  $\text{mV s}^{-1}$  (ESI S4.1 Fig. S4†). The obtained  $C_{\text{dl}}$  values for  $\text{MnCo}_2\text{O}_4$ -NiOOH, NiOOH, and  $\text{MnCo}_2\text{O}_4$  are 30, 8.1, and 5.8  $\text{mF cm}^{-2}$ , respectively (Fig. 4f). The significance of the electrochemical active surface area (ECSA) in the realm of electrocatalysis is underscored by various important factors. Gaining understanding of these concepts can offer valuable perspectives on the development and assessment of electrocatalysts. ECSA is a measure that accurately reflects the actual surface area of an electrode that is accessible for electrochemical processes. A higher ECSA value corresponds to an increased number of accessible sites for reactant molecules to adsorb and undergo the intended electrochemical transition. The pace at which these reactions occur is directly influenced by this factor, thereby impacting the overall efficiency and performance of the electrochemical system.

The electrochemically active surface area (ECSA) was computed from the  $C_{\text{dl}}$  values, and the obtained ECSA values for  $\text{MnCo}_2\text{O}_4$ -NiOOH, NiOOH, and  $\text{MnCo}_2\text{O}_4$  were 75, 20.25, and 14.5  $\text{cm}^2$ , respectively. A high ECSA value signifies that the catalytic surface contains a significant number of active sites. We also normalized the LSV curves of all the catalysts using ECSA, and the heterostructure is still highly active than that of the individual  $\text{MnCo}_2\text{O}_4$  and NiOOH phases (ESI S4.2 Fig. S6†). By comparing the amount of oxygen ( $\text{O}_2$ ) evolved experimentally with the theoretical amount of oxygen ( $\text{O}_2$ ) evolved, we can estimate the faradic efficiency using the water-gas displacement method. Our catalyst has a faradic efficiency of 98.5% (Fig. 4g). The chronoamperometry technique was utilized to investigate the long-term durability of the  $\text{MnCo}_2\text{O}_4$ -NiOOH catalyst for the OER. As can be observed in Fig. 4h, a continuous durability test lasting 140 hours was conducted with chronoamperometry at a very high current density of 300  $\text{mA cm}^{-2}$ . Based on the results of this experiment, the  $\text{MnCo}_2\text{O}_4$ -NiOOH catalyst is exceptionally stable even when subjected to harsh conditions. Comparing the activity of the majority of the reported  $\text{MnCo}_2\text{O}_4$ - and  $\text{Ni}_3\text{N}$ -based catalysts

(Fig. 4i), we observed that the present catalyst exhibits significantly low overpotential. The details of the catalyst documented here are provided in ESI S4.3 Table S1.†

To investigate the surface of the catalyst after a long-term durability test, we used the TEM and SEM techniques. The TEM image (Fig. 5a) shows the presence of  $\text{MnCo}_2\text{O}_4$  nanowires wrapped by NiOOH sheets. HRTEM analysis (Fig. 5b-d) also confirms the presence of  $\text{MnCo}_2\text{O}_4$  and NiOOH phases. The SEM images confirm the retention of the nano-urchin morphology (Fig. 5e-g). The elemental mapping of the catalyst after stability testing confirms the presence of Ni, Mn, Co, and O after the long-term durability tests (Fig. 5h-l). We also analysed the valence state of the elements present in the catalyst after the stability test. We did not find any change in the XPS spectra after the long-term durability test (ESI S4.4 Fig. S7†).

### DFT calculations

DFT modelling was used to provide an understanding of the precise mechanism underlying the OER. A theoretical model was constructed, as illustrated in Fig. 6a and b, to more effectively depict the synergistic action in  $\text{MnCo}_2\text{O}_4$ -NiOOH. Fig. 6c shows the OER process in an alkaline medium, which comprises four intermediates: (i)  $\text{OH}^*$  is adsorbed on the metal active site; (ii)  $\text{O}^*$  is formed; (iii)  $\text{OOH}^*$  is produced; (iv)  $\text{O}_2$  is evolved; and the active site is left unoccupied, which is employed for more oxygen evolution. In the ESI (ESI) section S5, Tables S2–S5† contain a description of how the adsorption energy was calculated. The projected orbital density of state (DOS) plots for the d-orbitals are shown in Fig. 6d. The area under the curve embodies the number of occupied electronic states at each energy level. It was observed that  $\text{MnCo}_2\text{O}_4$ -NiOOH exhibits a considerably larger density of states at the Fermi level as compared to  $\text{MnCo}_2\text{O}_4$  and NiOOH individually. This substantial increase in the density of states of the d-orbitals at the Fermi level after introducing NiOOH into  $\text{MnCo}_2\text{O}_4$  leads to faster and more efficient charge transfer. Additionally, the significant active site in the process of catalyzing the OER was identified by computing the change in Gibbs free energy ( $\Delta G$ ) of each elementary step of the catalyst. Fig. 6e and f present the  $\Delta G$  value (at  $U = 1.23 \text{ V}$  and  $0 \text{ V}$ ) of the catalyst. It was found that the  $\Delta G$  value of the rate-limiting step (RLS) is lower in the case of  $\text{MnCo}_2\text{O}_4$ -Ni\*OOH (1.03 V) as compared to those of  $\text{Mn}^*\text{Co}_2\text{O}_4$  (2.55 V),  $\text{MnCo}^*\text{O}_4$  (1.63 V), and  $\text{Ni}^*\text{OOH}$  (1.23 V) (\* signifies the catalyst site). The analysis revealed that the incorporation of NiOOH into the  $\text{MnCo}_2\text{O}_4$  decreased the  $\Delta G$  value of the RLS, and the rate of reaction increased.

### Overall water splitting activity

Motivated by the favourable oxygen evolution reaction (OER) activity, the  $\text{MnCo}_2\text{O}_4$ -NiOOH composite was utilized as an anode, and Pt/C was used as the cathode, in order to evaluate the water splitting performance. Fig. 7a shows a schematic representation of the Pt/C|| $\text{MnCo}_2\text{O}_4$ -NiOOH cell. We obtained a very low cell potential of 1.46 V to drive a current density of 10  $\text{mA cm}^{-2}$ , which is superior to that of Pt/C|| $\text{RuO}_2$  (Fig. 7b).

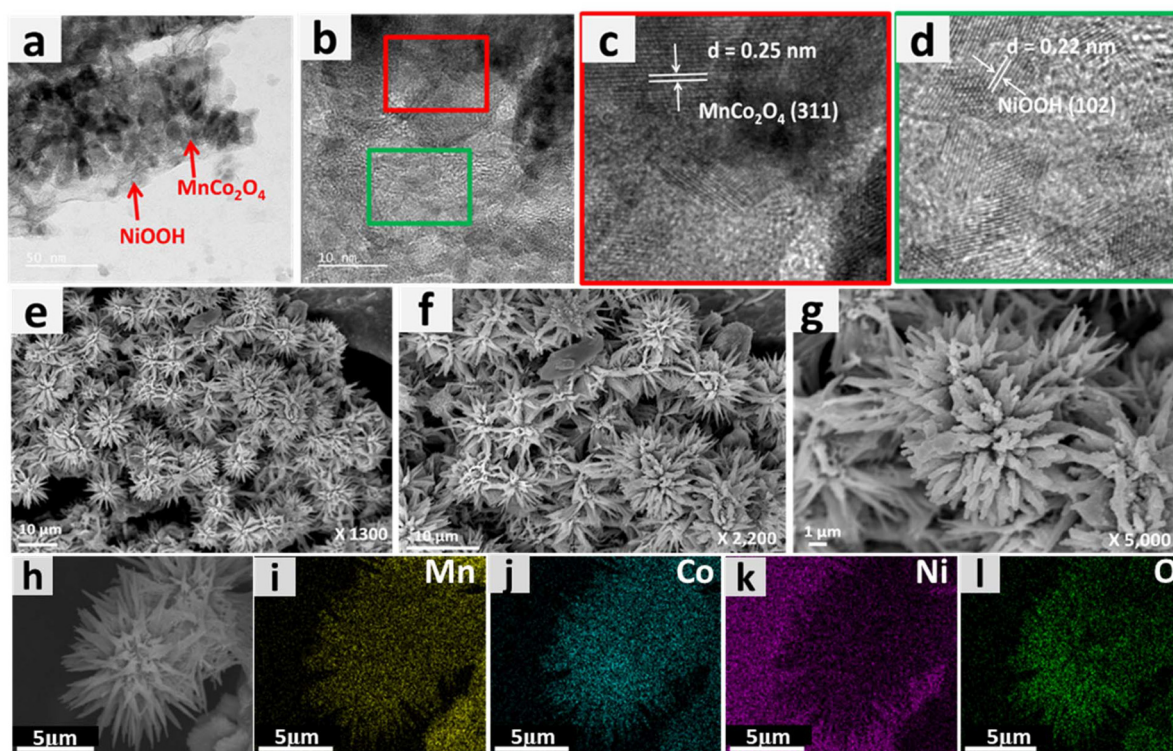


Fig. 5 (a) TEM image after the durability test. (b), (c) and (d) HRTEM images after the durability test confirming the presence of (c) MnCo<sub>2</sub>O<sub>4</sub> and (d) NiOOH. (e–g) FESEM images of MnCo<sub>2</sub>O<sub>4</sub>–NiOOH after the durability test. (h–l) FESEM elemental mapping of the catalyst after the durability test.

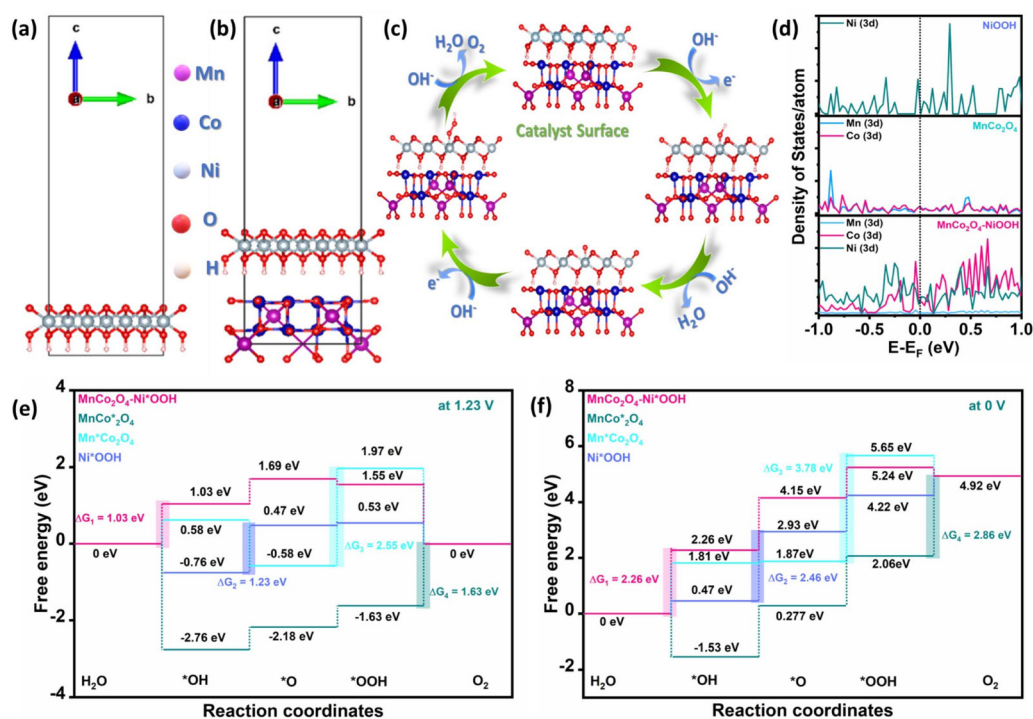
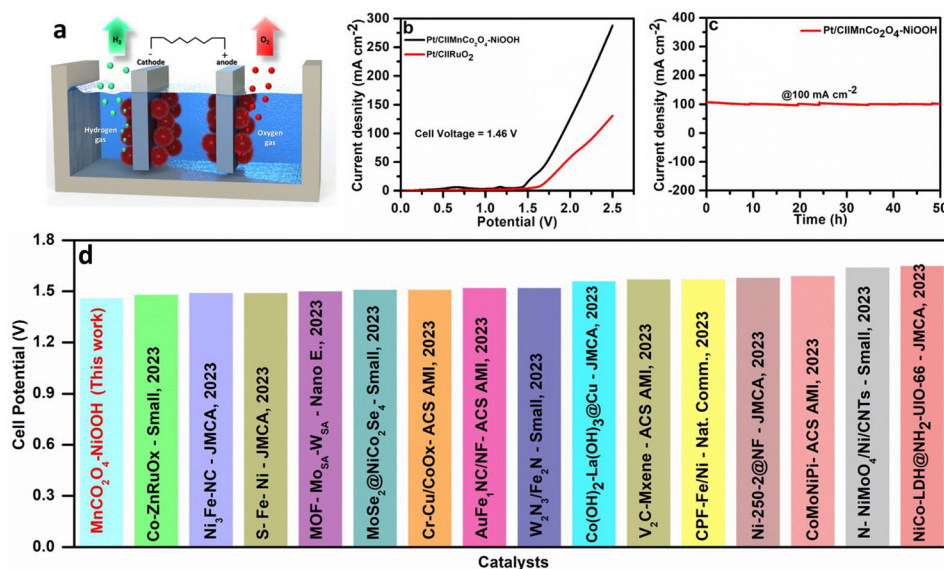


Fig. 6 Theoretical models of (a) MnCo<sub>2</sub>O<sub>4</sub> and (b) MnCo<sub>2</sub>O<sub>4</sub>–NiOOH. (c) illustration of the mechanism for the OER on the heterostructure (d) Projected orbital DOS plot. Gibbs free energy plot for the OER (e) at 1.23 V and (f) at 0 V for MnCo<sub>2</sub>O<sub>4</sub>, NiOOH, and MnCo<sub>2</sub>O<sub>4</sub>–NiOOH.





**Fig. 7** (a) Schematic representation of the cell for overall water splitting. (b) LSV curve in two-electrode setup. (c) Durability test using chronoamperometry. (d) Comparison of cell potential with the cell potentials of recently reported catalysts.

The catalyst was also stable for 50 h, showing a continuous current density of  $100 \text{ mA cm}^{-2}$  (Fig. 7c). Additionally, this performance surpasses the majority of recently reported catalysts that do not contain noble metals (Fig. 7d). The details of the catalyst documented here are provided in ESI S6 Table S2.†

## Conclusions

In summary, the heterostructure  $\text{MnCo}_2\text{O}_4\text{-Ni}_3\text{N}$  shows rapid phase transformation to form  $\text{MnCo}_2\text{O}_4\text{-NiOOH}$ . The rapid phase transformation was governed by the strong coupling effect between  $\text{MnCo}_2\text{O}_4$  and  $\text{Ni}_3\text{N}$ , which results in electronic reallocation through the interface. The catalyst  $\text{MnCo}_2\text{O}_4\text{-NiOOH}$  exhibits an overpotential of 224 mV and is far superior to  $\text{MnCo}_2\text{O}_4$  or  $\text{NiOOH}$  alone. The electronic reallocation was extensively examined using X-ray photoelectron spectroscopy (XPS), which revealed a shift towards higher binding energy for Ni and N and towards lower binding energy for Mn, Co, and O. The  $\text{MnCo}_2\text{O}_4\text{-NiOOH}$  heterostructure shows stability for up to 140 h at a high current density of  $300 \text{ mA cm}^{-2}$ . The DFT studies also revealed that the  $\text{NiOOH}$  formed over the  $\text{MnCo}_2\text{O}_4$  nanowires is more active than that of  $\text{NiOOH}$  alone. Nanostructures with carefully engineered interfaces are a necessary step in developing cutting-edge methods for energy conversion.

## Author contributions

V. B. and A. G. thought of the idea for this piece of work. A. G. and J. M. J. did the synthesis and performed the detailed characterization. A. A. and C. B. performed the theoretical calculations. J. S., V. P., R. K. and K. G. helped in the data ana-

lysis and representation. A. G. and V. B. wrote the manuscript. The final draft of the article has been reviewed and approved by all authors.

## Conflicts of interest

There are no conflicts to declare.

## Acknowledgements

A. G., A. A. and V. P. thank INST for providing fellowships. V. B. acknowledges DST SERB (CRG/2022/006402).

## References

- 1 D. C. R. Hans-Otto Pörtner, M. M. B. Tignor, E. Poloczanska, K. Mintenbeck, A. Alegría, M. Craig, S. Langsdorf, S. Löschke, V. Möller, A. Okem and B. Rama, Contribution to the Sixth Assessment Report of the Intergovernmental Panel on Climate Change, *Climate Change 2022: Impacts, Adaptation and Vulnerability*, 2022, p. 3005.
- 2 L. Li, P. Wang, Q. Shao and X. Huang, Metallic nanostructures with low dimensionality for electrochemical water splitting, *Chem. Soc. Rev.*, 2020, **49**(10), 3072–3106.
- 3 B. Zhang, Y. Zheng, T. Ma, C. Yang, Y. Peng, Z. Zhou, M. Zhou, S. Li, Y. Wang and C. Cheng, Designing MOF Nanoarchitectures for Electrochemical Water Splitting, *Adv. Mater.*, 2021, **33**(17), 2006042.
- 4 E. Enkhtuvshin, S. Yeo, H. Choi, K. M. Kim, B.-S. An, S. Biswas, Y. Lee, A. K. Nayak, J. U. Jang, K.-H. Na,

- W.-Y. Choi, G. Ali, K. H. Chae, M. Akbar, K. Y. Chung, K. Yoo, Y.-C. Chung, T. H. Shin, H. Kim, C.-Y. Chung and H. Han, Surface Reconstruction of Ni-Fe Layered Double Hydroxide Inducing Chloride Ion Blocking Materials for Outstanding Overall Seawater Splitting, *Adv. Funct. Mater.*, 2023, **33**(22), 2214069.
- 5 H. Han, S. J. Kim, S. Y. Jung, D. Oh, A. K. Nayak, J. U. Jang, J. Bang, S. Yeo and T. H. Shin, Amorphous-Crystalline Interfaces on Hollow Nanocubes Derived from Ir-Doped Ni-Fe-Zn Prussian Blue Analog Enables High Capability of Alkaline/Acidic/Saline Water Oxidations, *Small*, 2023, 2303912.
  - 6 R. R. Rao, I. E. L. Stephens and J. R. Durrant, Understanding What Controls the Rate of Electrochemical Oxygen Evolution, *Joule*, 2021, **5**(1), 16–18.
  - 7 J. Wang, S.-J. Kim, J. Liu, Y. Gao, S. Choi, J. Han, H. Shin, S. Jo, J. Kim, F. Ciucci, H. Kim, Q. Li, W. Yang, X. Long, S. Yang, S.-P. Cho, K. H. Chae, M. G. Kim, H. Kim and J. Lim, Redirecting dynamic surface restructuring of a layered transition metal oxide catalyst for superior water oxidation, *Nat. Catal.*, 2021, **4**(3), 212–222.
  - 8 C. Baeumer, J. Li, Q. Lu, A. Y.-L. Liang, L. Jin, H. P. Martins, T. Duchoň, M. Glöß, S. M. Gericke, M. A. Wohlgemuth, M. Giesen, E. E. Penn, R. Dittmann, F. Gunkel, R. Waser, M. Bajdich, S. Nemsák, J. T. Mefford and W. C. Chueh, Tuning electrochemically driven surface transformation in atomically flat LaNiO<sub>3</sub> thin films for enhanced water electrolysis, *Nat. Mater.*, 2021, **20**(5), 674–682.
  - 9 C. Lei, Q. Zheng, F. Cheng, Y. Hou, B. Yang, Z. Li, Z. Wen, L. Lei, G. Chai and X. Feng, High-Performance Metal-Free Nanosheets Array Electrocatalyst for Oxygen Evolution Reaction in Acid, *Adv. Funct. Mater.*, 2020, **30**(31), 2003000.
  - 10 H. B. Tao, Y. Xu, X. Huang, J. Chen, L. Pei, J. Zhang, J. G. Chen and B. Liu, A General Method to Probe Oxygen Evolution Intermediates at Operating Conditions, *Joule*, 2019, **3**(6), 1498–1509.
  - 11 Y. Liu, Y. Wang, S. Zhao and Z. Tang, Metal–Organic Framework-Based Nanomaterials for Electrocatalytic Oxygen Evolution, *Small Methods*, 2022, **6**(10), 2200773.
  - 12 S. Zhao, Y. Yang and Z. Tang, Insight into Structural Evolution, Active Sites, and Stability of Heterogeneous Electrocatalysts, *Angew. Chem., Int. Ed.*, 2022, **61**(11), e202110186.
  - 13 W. Cheng, X. Zhao, H. Su, F. Tang, W. Che, H. Zhang and Q. Liu, Lattice-strained metal–organic-framework arrays for bifunctional oxygen electrocatalysis, *Nat. Energy*, 2019, **4**(2), 115–122.
  - 14 A. Joshi, P. Sood, A. Gaur, D. Rani, V. Madaan and M. Singh, Improved OER performance of an Anderson-supported cobalt coordination polymer by assembling with acetylene black, *J. Mater. Chem. A*, 2022, **10**(24), 12805–12810.
  - 15 I. Yamada, H. Fujii, A. Takamatsu, H. Ikeno, K. Wada, H. Tsukasaki, S. Kawaguchi, S. Mori and S. Yagi, Bifunctional Oxygen Reaction Catalysis of Quadruple Manganese Perovskites, *Adv. Mater.*, 2017, **29**(4), 1603004.
  - 16 Y. Zhou, S. Sun, C. Wei, Y. Sun, P. Xi, Z. Feng and Z. J. Xu, Significance of Engineering the Octahedral Units to Promote the Oxygen Evolution Reaction of Spinel Oxides, *Adv. Mater.*, 2019, **31**(41), 1902509.
  - 17 A. K. Shah and M. Qureshi, In Situ Grown Cuboidal MnCo<sub>2</sub>O<sub>4</sub>/h Boron Nitride Heterojunction: A Noble Metal-Free Approach Based on Efficient Hole Extraction for Electrochemical Oxygen Evolution Reaction, *ACS Appl. Energy Mater.*, 2022, **5**(2), 1551–1559.
  - 18 J. Y. C. Chen, J. T. Miller, J. B. Gerken and S. S. Stahl, Inverse spinel NiFeAlO<sub>4</sub> as a highly active oxygen evolution electrocatalyst: promotion of activity by a redox-inert metal ion, *Energy Environ. Sci.*, 2014, **7**(4), 1382–1386.
  - 19 H. Han, Y. Qiu, H. Zhang, T. Bi, Q. Yang, M. Liu, J. Zhou and X. Ji, Lattice-disorder layer generation from liquid processing at room temperature with boosted nanointerface exposure toward water splitting, *Sustainable Energy Fuels*, 2022, **6**(12), 3008–3013.
  - 20 Y. Qiu, Z. Liu, Q. Yang, X. Zhang, J. Liu, M. Liu, T. Bi and X. Ji, Atmospheric-Temperature Chain Reaction towards Ultrathin Non-Crystal-Phase Construction for Highly Efficient Water Splitting, *Chem. – Eur. J.*, 2022, **28**(51), e202200683.
  - 21 J. Luo, X. Wang, Y. Gu, D. Wang, S. Wang, W. Li, Y. Zhou and J. Zhang, Constructing hollow nanocages of Co<sub>3</sub>O<sub>4</sub>-CoMoO<sub>4</sub> heterostructure for efficient electrocatalytic oxygen evolution reaction, *Appl. Surf. Sci.*, 2022, **606**, 154562.
  - 22 Y. Pan, H. Ren, R. Chen, Y. Wu and D. Chu, Enhanced electrocatalytic oxygen evolution by manipulation of electron transfer through cobalt-phosphorous bridging, *Chem. Eng. J.*, 2020, **398**, 125660.
  - 23 D. Gao, J. Zhang, T. Wang, W. Xiao, K. Tao, D. Xue and J. Ding, Metallic Ni<sub>3</sub>N nanosheets with exposed active surface sites for efficient hydrogen evolution, *J. Mater. Chem. A*, 2016, **4**(44), 17363–17369.
  - 24 B. You, X. Liu, G. Hu, S. Gul, J. Yano, D.-e. Jiang and Y. Sun, Universal Surface Engineering of Transition Metals for Superior Electrocatalytic Hydrogen Evolution in Neutral Water, *J. Am. Chem. Soc.*, 2017, **139**(35), 12283–12290.
  - 25 K. Xu, P. Chen, X. Li, Y. Tong, H. Ding, X. Wu, W. Chu, Z. Peng, C. Wu and Y. Xie, Metallic Nickel Nitride Nanosheets Realizing Enhanced Electrochemical Water Oxidation, *J. Am. Chem. Soc.*, 2015, **137**(12), 4119–4125.
  - 26 Z. Liu, M. Zha, Q. Wang, G. Hu and L. Feng, Overall water-splitting reaction efficiently catalyzed by a novel bi-functional Ru/Ni<sub>3</sub>N–Ni electrode, *Chem. Commun.*, 2020, **56**(15), 2352–2355.
  - 27 M. Wang, W. Ma, Z. Lv, D. Liu, K. Jian and J. Dang, Co-Doped Ni<sub>3</sub>N Nanosheets with Electron Redistribution as Bifunctional Electrocatalysts for Efficient Water Splitting, *J. Phys. Chem. Lett.*, 2021, **12**(6), 1581–1587.
  - 28 A. Wu, Y. Xie, H. Ma, C. Tian, Y. Gu, H. Yan, X. Zhang, G. Yang and H. Fu, Integrating the active OER and HER components as the heterostructures for the efficient overall water splitting, *Nano Energy*, 2018, **44**, 353–363.

- 29 A. Gaur, J. M. John, V. Pundir, R. Kaur and V. Bagchi, Electronegativity-Induced Valence State Augmentation of Ni and Co through Electronic Redistribution between Co-Ni<sub>3</sub>N/CeF<sub>3</sub> Interfaces for Oxygen Evolution Reaction, *ACS Appl. Energy Mater.*, 2023, **6**(3), 1763–1770.
- 30 C. Ray, S. C. Lee, B. Jin, A. Kundu, J. H. Park and S. Chan Jun, Conceptual design of three-dimensional CoN/Ni<sub>3</sub>N-coupled nanograsses integrated on N-doped carbon to serve as efficient and robust water splitting electrocatalysts, *J. Mater. Chem. A*, 2018, **6**(10), 4466–4476.
- 31 X. Gao, X. Liu, W. Zang, H. Dong, Y. Pang, Z. Kou, P. Wang, Z. Pan, S. Wei, S. Mu and J. Wang, Synergizing in-grown Ni<sub>3</sub>N/Ni heterostructured core and ultrathin Ni<sub>3</sub>N surface shell enables self-adaptive surface reconfiguration and efficient oxygen evolution reaction, *Nano Energy*, 2020, **78**, 105355.
- 32 M. Zhao, W. Yuan and C. M. Li, Controlled self-assembly of Ni foam supported poly (ethyleneimine)/reduced graphene oxide three-dimensional composite electrodes with remarkable synergistic effects for efficient oxygen evolution, *J. Mater. Chem. A*, 2017, **5**(3), 1201–1210.
- 33 F. Wang, G. Chen, X. Liu, F. Chen, H. Wan, L. Ni, N. Zhang, R. Ma and G. Qiu, Advanced Electrocatalytic Performance of Ni-Based Materials for Oxygen Evolution Reaction, *ACS Sustainable Chem. Eng.*, 2019, **7**(1), 341–349.
- 34 Q. Zhou, T.-T. Li, F. Guo and Y.-Q. Zheng, Construction of Hierarchically Structured CuO@CoP Anode for Efficient Oxygen Evolution Reaction, *ACS Sustainable Chem. Eng.*, 2018, **6**(9), 11303–11312.
- 35 J. Luo, X. H. Wang, L. Shen, H. C. Fu, X. H. Chen, L. L. Wu, Q. Zhang, H. Q. Luo and N. B. Li, Corrosion-Engineered Mo-Containing FeCo-(oxy)hydroxide Electrocatalysts for Superior Oxygen Evolution Reaction, *ACS Sustainable Chem. Eng.*, 2021, **9**(36), 12233–12241.
- 36 S. Sirisomboonchai, S. Li, A. Yoshida, X. Li, C. Samart, A. Abudula and G. Guan, Fabrication of NiO Microflake@NiFe-LDH Nanosheet Heterostructure Electrocatalysts for Oxygen Evolution Reaction, *ACS Sustainable Chem. Eng.*, 2019, **7**(2), 2327–2334.
- 37 M. Zhao, H. Li, W. Yuan and C. M. Li, Tannic acid-mediated in situ controlled assembly of NiFe alloy nanoparticles on pristine graphene as a superior oxygen evolution catalyst, *ACS Appl. Energy Mater.*, 2020, **3**(4), 3966–3977.
- 38 J. Bai, J. Mei, T. Liao, Q. Sun, Z.-G. Chen and Z. Sun, Molybdenum-Promoted Surface Reconstruction in Polymorphic Cobalt for Initiating Rapid Oxygen Evolution, *Adv. Energy Mater.*, 2022, **12**(5), 2103247.
- 39 C. Wang, P. Zhai, M. Xia, W. Liu, J. Gao, L. Sun and J. Hou, Identification of the Origin for Reconstructed Active Sites on Oxyhydroxide for Oxygen Evolution Reaction, *Adv. Mater.*, 2023, **35**(6), 2209307.
- 40 J. Zhang, W. He, H. B. Aiyappa, T. Quast, S. Dieckhöfer, D. Öhl, J. R. C. Junqueira, Y.-T. Chen, J. Masa and W. Schuhmann, Hollow CeO<sub>2</sub>@Co<sub>2</sub>N Nanosheets Derived from Co-ZIF-L for Boosting the Oxygen Evolution Reaction, *Adv. Mater. Interfaces*, 2021, **8**(9), 2100041.
- 41 J. Ge, W. Zhang, J. Tu, T. Xia, S. Chen and G. Xie, Suppressed Jahn–Teller Distortion in MnCo<sub>2</sub>O<sub>4</sub>@Ni<sub>2</sub>P Heterostructures to Promote the Overall Water Splitting, *Small*, 2020, **16**(34), 2001856.
- 42 J. Sun, J. Lu, C. Huang, Q. Wu, L. Xia, Q. Xu and W. Yao, Modification of Ni<sub>3</sub>N with a Cobalt-Doped Carbon Shell for High-Performance Hydrogen Evolution in Alkaline Media, *ACS Sustainable Chem. Eng.*, 2021, **9**(5), 1994–2002.
- 43 G. S. Shanker and S. Ogale, Faceted Colloidal Metallic Ni<sub>3</sub>N Nanocrystals: Size-Controlled Solution-Phase Synthesis and Electrochemical Overall Water Splitting, *ACS Appl. Energy Mater.*, 2021, **4**(3), 2165–2173.
- 44 Y. Yang, Q. Dai, L. Shi, Y. Liu, T. T. Isimjan and X. Yang, Electronic Modulation of Pt Nanoparticles on Ni<sub>3</sub>N–Mo<sub>2</sub>C by Support-Induced Strategy for Accelerating Hydrogen Oxidation and Evolution, *J. Phys. Chem. Lett.*, 2022, **13**(9), 2107–2116.
- 45 M. Yang, M. Zhao, J. Yuan, J. Luo, J. Zhang, Z. Lu, D. Chen, X. Fu, L. Wang and C. Liu, Oxygen Vacancies and Interface Engineering on Amorphous/Crystalline CrOx–Ni<sub>3</sub>N Heterostructures toward High-Durability and Kinetically Accelerated Water Splitting, *Small*, 2022, **18**(14), 2106554.
- 46 Y. Chen, J. Yu, J. Jia, F. Liu, Y. Zhang, G. Xiong, R. Zhang, R. Yang, D. Sun, H. Liu and W. Zhou, Metallic Ni<sub>3</sub>Mo<sub>3</sub>N Porous Microrods with Abundant Catalytic Sites as Efficient Electrocatalyst for Large Current Density and Superstability of Hydrogen Evolution Reaction and Water Splitting, *Appl. Catal., B*, 2020, **272**, 118956.
- 47 L. Qi, Z. Zheng, C. Xing, Z. Wang, X. Luan, Y. Xue, F. He and Y. Li, 1D Nanowire Heterojunction Electrocatalysts of MnCo<sub>2</sub>O<sub>4</sub>/GDY for Efficient Overall Water Splitting, *Adv. Funct. Mater.*, 2022, **32**(11), 2107179.
- 48 K. Zeng, W. Li, Y. Zhou, Z. Sun, C. Lu, J. Yan, J.-H. Choi and R. Yang, Multilayer hollow MnCo<sub>2</sub>O<sub>4</sub> microsphere with oxygen vacancies as efficient electrocatalyst for oxygen evolution reaction, *Chem. Eng. J.*, 2021, **421**, 127831.
- 49 T.-H. Ko, K. Devarayan, M.-K. Seo, H.-Y. Kim and B.-S. Kim, Facile Synthesis of Core/Shell-like NiCo<sub>2</sub>O<sub>4</sub>-Decorated MWCNTs and its Excellent Electrocatalytic Activity for Methanol Oxidation, *Sci. Rep.*, 2016, **6**(1), 20313.
- 50 J. F. Marco, J. R. Gancedo, M. Gracia, J. L. Gautier, E. Ríos and F. J. Berry, Characterization of the Nickel Cobaltite, NiCo<sub>2</sub>O<sub>4</sub>, Prepared by Several Methods: An XRD, XANES, EXAFS, and XPS Study, *J. Solid State Chem.*, 2000, **153**(1), 74–81.
- 51 Y. Mo, Q. Ru, X. Song, S. Hu, L. Guo and X. Chen, 3-dimensional porous NiCo<sub>2</sub>O<sub>4</sub> nanocomposite as a high-rate capacity anode for lithium-ion batteries, *Electrochim. Acta*, 2015, **176**, 575–585.
- 52 R. Andaveh, G. Barati Darband and M. Maleki, Sabour Rouhaghdam, A., Superaerophobic/superhydrophilic surfaces as advanced electrocatalysts for the hydrogen evolution reaction: a comprehensive review, *J. Mater. Chem. A*, 2022, **10**(10), 5147–5173.



- 53 Q. Hu, G. Li, X. Liu, B. Zhu, X. Chai, Q. Zhang, J. Liu and C. He, Superhydrophilic Phytic-Acid-Doped Conductive Hydrogels as Metal-Free and Binder-Free Electrocatalysts for Efficient Water Oxidation, *Angew. Chem., Int. Ed.*, 2019, **58**(13), 4318–4322.
- 54 A. Gaur, Krishankant, V. Pundir, A. Singh, T. Maruyama, C. Bera and V. Bagchi, Intense nano-interfacial interactivity stimulates the OER in a MOF-derived superhydrophilic CuO–NiO heterostructure, *Sustainable Energy Fuels*, 2021, **5**(21), 5505–5512.